

Microscopic Imaging and Optical Pressure Measurements of Detonations

I. Emre Gunduz^{*,[a, b]}

Abstract: The microstructure of solid high explosives can affect their safety and performance. However, the extreme conditions in the vicinity of detonating explosives make high-resolution imaging and data acquisition challenges. A new diagnostic method is presented here that allows microscopic imaging of self-supported detonations while optically measuring pressures in an arbitrary confiner material nearby using an imaging fiber and an image intensifier at a safe distance. Tests with pressed pellets of HMX and PBX

9501 revealed features during pore collapse in engineered holes and detonation reaction zone morphology and thickness. Interface experiments allowed the measurement of pressure at the boundary between the explosive and a silicone polymer and the determination of the specific heat ratio for the gaseous products. The same methodology can be used to fit any form of equation-of-state and Hugoniot curves for arbitrary materials using few simple experiments.

Keywords: high explosive · detonation · imaging · optical · high speed

1 Introduction

Detonations in solid explosives are produced by the rapid conversion of the solid into a large volume of gaseous products starting at the shock fronts that move at supersonic speeds [1,2]. As the shock compresses and heats the explosive, it initiates reactions and generates more heat and gas, resulting in shock propagation. The characteristic properties of detonations of high explosives (HE) like Octahydro-1,3,5,7-tetranitro-1,3,5,7-tetrazocine (HMX) depend on properties such as density, porosity, detonation temperature, speed of sound, reaction rates, and volume of gases generated. Heterogeneous HEs such as PBX 9501 comprise a polymeric binder that holds together the HE particles (95% HMX for PBX 9501). Due to their inhomogeneity at small scales, their detonation characteristics, initiation, and sensitivity can be influenced by their microstructural features [1–5].

The shock waves and hot expanding products from HE detonations also interact with the surrounding medium depending on its density. For example, air or polymers offer little inertial resistance to the gaseous products that can expand more readily, compared to denser mediums such as metals that provide stronger confinement. These interactions are exploited in applications such as mining and welding [2]. Figure 1A shows a high-speed camera frame (50 ns exposure) from a detonating 6 mm diameter cylindrical HMX HE pellet, where the dotted lines show the remaining unreacted part. The corresponding detonation front structure for the HMX with weak (air) confinement in a cylindrical configuration is shown in Figure 1B adapted from [6,7] along with the pressure variation across the pellet based on the Zel'dovich-Von Neumann-Döring (ZND) model [8] (Figure 1C). The supersonic shock leads ahead a steady reaction zone (RZ), where re-

actants form high-pressure gaseous products. The maximum pressure (i.e. Von Neumann spike) occurs at the leading shock boundary. The pressure gradually drops in the RZ and the ideal 1D case, the reactants are completely consumed at the trailing sonic surface, where the Chapman-Jouguet (CJ) condition is satisfied [2,9]. CJ state is derived from the conservation of mass, momentum, and energy between the reactants and the products across the detonation front at the sonic surface. For the weak confinement case shown, the sonic surface intersects the detonation shock at the material interface, but the reaction zone can extend further downstream [6,10]. This increases the width of the reaction zone along with the interfaces with the confiner. The gases generated expand behind the front and depending on the chemistry and the oxygen balance of the HE, products can further react with oxygen in air or undergo phase transformations. However, these do not contribute to the DDZ since they trail behind it at subsonic speeds.

The nature of detonations has always invoked great interest and prompted the development of many diagnostic techniques. These include high-speed imaging systems that started with the rapid collection of analog photographs for imaging nuclear explosions and other rapid events [11]. These

[a] I. E. Gunduz
Mechanical and Aerospace Engineering Department,
Naval Postgraduate School,
Monterey CA 93943, USA
*e-mail: emre.gunduz@nps.edu

[b] I. E. Gunduz
School of Mechanical Engineering,
Purdue University, West Lafayette
IN 47907, USA

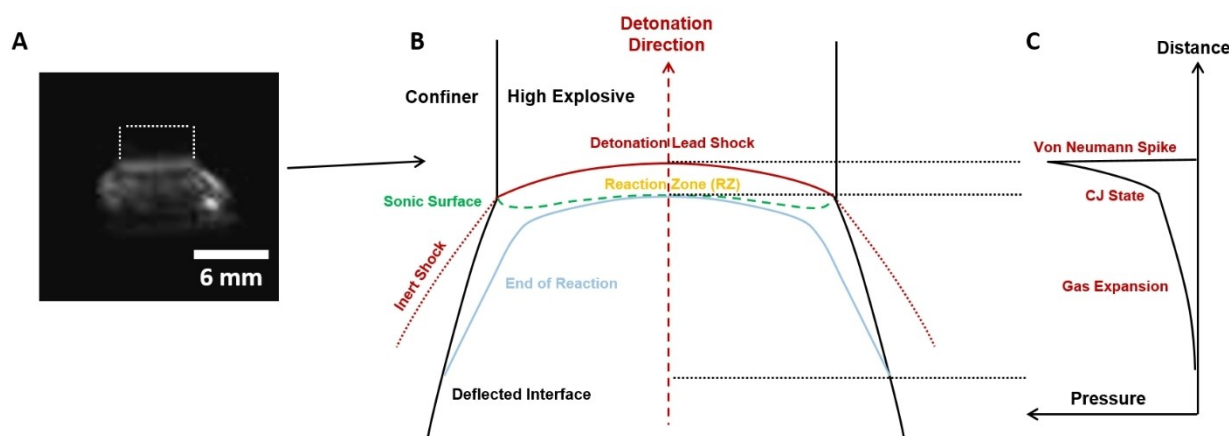


Figure 1. (A) A single frame (50 ns exposure) from a detonating high explosive cylindrical pellet with a diameter of 6 mm (dotted lines show the remaining part of the pellet). (B) A schematic of the detonation front in a high explosive and a confiner interface adapted from [6] in a cylindrical configuration with weak confinement and (C) the corresponding pressure at the center of the pellet based on the Zel'dovich-Von Neumann-Döring (ZND) model.

analog framing cameras evolved into digital systems with very high speeds that are much simpler to use. The commercially available state-of-the-art cameras have imaging rates in the range of 1 to 1000 Million frames per second (Mfps) with a correspondingly decreasing number of acquired frames. These systems have been used for the direct imaging of detonations at relatively low spatial resolutions (100 $\mu\text{m}/\text{pixel}$) due to the required safe working distance [12]. However, for the case of small thin (100–200 μm) vapor-deposited samples of Pentaerythritoltetranitrate (PETN) and hexanitroazobenzene (HNAB), these systems have been used successfully at a high resolution of 4–5 $\mu\text{m}/\text{pixel}$ permitted by the very small amount (< 100 μg) of material used [13]. Streak cameras have long been used in detonation experiments due to the very high acquisition speeds available for imaging series of 1D images with less than picosecond frame times. These can provide valuable 1D information on the front curvature [3,6], temperatures, and species evolution using bandpass filters. A variant of this approach includes the use of multiple fiber optic commercial fibers to distribute 2D pixel locations to the 1D window of a streak camera to get a broader field of view than a single line while retaining the extremely high temporal resolution with reported resolutions down to about 50–100 $\mu\text{m}/\text{pixel}$ [14,15]. Non-optical methods include proton radiography (PR) and flash x-ray imaging. For example, PR experiments on PBX 9502 confined between plates of PMMA with 304 stainless steel demonstrated good agreement with computational results [16]. A major disadvantage of PR is its limited resolution and difficulties in its implementation. Flash X-ray diagnostics can provide similar single-shot images from explosive events [17], but they suffer from the low resolution and noise level limit imposed by the limited flux at very short exposures. The use of high-flux synchrotron X-ray radiation can allow the phase-contrast imaging of explosives at high

speeds, albeit being limited to observing only the density variations in the detonation fronts [18].

High-speed imaging has also been used to study shock initiation. It is long been known that energy localization at hotspots can precede the initiation of a detonation event [1]. The microstructural inhomogeneities and interfaces common to pressed explosives can result in a rough shock profile with hotspots [3,4]. If critical conditions are present, these hotspots coalesce, resulting in either a detonation or a deflagration event. Possible mechanisms of hotspot formation include adiabatic heating due to void collapse and frictional heating at grain boundaries. Such phenomena can occur at very small scales down to a few micrometers [4] and require high-resolution imaging systems.

The morphology of the HE-confiner interfaces can yield valuable information. Using shock polar matching theory, relationships for detonation velocity and pressure as functions of the streamline deflection angle that is formed at the material and an inert confiner interface can be determined [6,7,19–21]. For example, 1D imaging with a streak camera has been used to perform Hugoniot measurements based on shock polar analysis [22].

The challenges in characterizing these high-speed (> 8 km/s) events at high spatial and temporal resolution arise from the extreme conditions in their vicinity. Microscopic imaging lenses require very short working distances to obtain high magnification, which can damage the expensive imaging equipment used. The exposure times have to be very short (~ 10 ns) to prevent motion blur at high spatial resolutions. In this work, we present an experimental technique that can overcome some of these issues, providing single frame microscopic images of (a) the HE detonation front structures from which a hotspot and reaction zone widths can be identified across a large field of view, (b) shock propagation across through-holes in PBX9501 pellets and (c) the detonation wave

driving an oblique shock at an interface into an inert material from which pressure at the material interface can be determined optically using oblique wave shock polar analysis. The system uses an imaging fiber bundle with 10000 individual $4.5\text{ }\mu\text{m}$ diameter optical fibers coupled to an image intensifier using a microscope objective. The use of the imaging fiber allows image acquisition at an imaging lens working distance of 40 mm, producing a pixel resolution of $15\text{ }\mu\text{m}$. The intensifier gate time of 10 ns gives an effective frame rate of 100 Mfps and reduces motion blur while the intensifier and the camera are 1.2 m away behind a blast shield for protection. The same events were also recorded simultaneously using a separate high-speed camera at 10 Mfps at an exposure of 50 ns at a low-resolution to provide a wider field of view images to aid in the interpretation of the high-resolution images (Figure 2).

2 Materials and Methods

The PBX 9501 and HMX particles used were both supplied by BAE Systems. The explosives were remotely pressed into pellets of specified heights using hardened steel dies and shims in a Carver press. The HMX pellet was cylindrical with a diameter and height of 6 mm. The PBX 9501 pellets were in the form of rectangular prisms with a length and width of 6 mm and a nominal height of 4 mm. The shape was chosen to be able to observe the detonation front curvature after the initial tests with cylindrical samples, which have radial symmetry. The PBX 9501 pellets were pressed to approximately 98% of their theoretical maximum density (TMD), while the HMX pellets were pressed to approximately 95% TMD. The estimated detonation speeds are 8.6 and 8.4 km/s for HMX and PBX 9501 respectively at these densities. Additionally, 500 μm diameter through-holes were drilled in the PBX 9501 samples using a fine drill bit. A sharpie marker was used to make ink markings next to the engineered holes to aid in focusing. Three experiments with varying delays were performed with

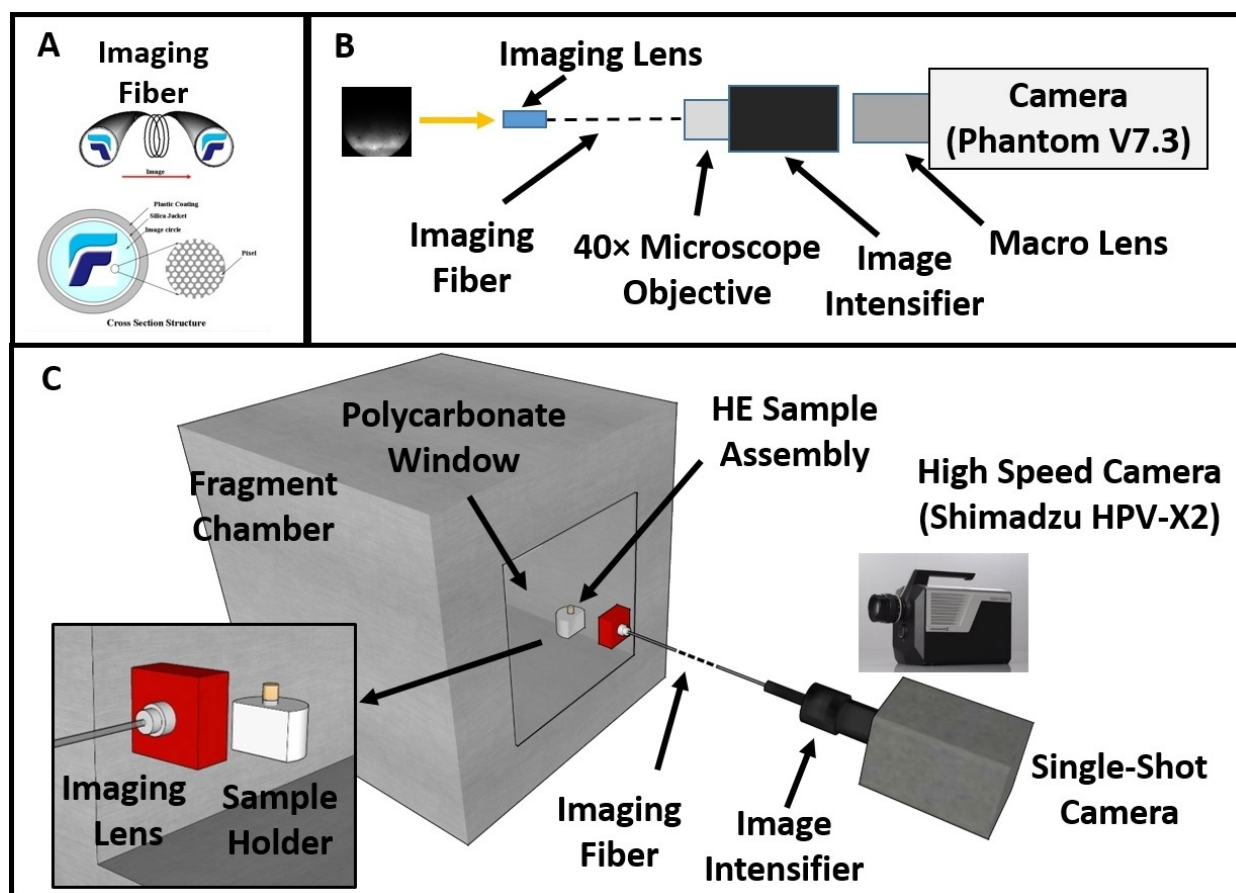


Figure 2. A. Imaging fiber consists of multiple fibers that preserve images during transmission. B. High magnification imaging assembly, where an imaging fiber is attached to an image intensifier with coupling optics that is imaged by a Phantom V7.3 black and white high speed camera for single-shot images. C. The schematic for the setup showing the sample within the fragment chamber that is imaged using two cameras behind a polycarbonate window. The imaging fiber length is not to scale; the cameras are located further back at a distance of approximately 1.2 m. The fiber lens is 40 mm away from the HE sample.

the PBX 9501 samples to observe the interaction of the detonation front with the holes. The required delays were calculated by measuring the distance between the initiator and the hole in the explosive pellet and using the detonation speed to calculate the time it takes for the front to reach the hole. The estimated detonation speeds were consistent with the delays required for imaging. For the interface experiment with the explosive and inert material, a Sylgard 184 (Dow Corning) block with the same size as the PBX 9501 pellet was attached to one of the side walls using a very thin layer of silicone vacuum grease that was not visible in any of the images. The density of Sylgard 184 after curing is reported as 1.03 g cm^{-3} by the manufacturer.

The overall setup is shown in Figure 2C. The pellets were attached on top of RP-502 exploding bridge-wire (EBW) detonators using a thin layer of silicone vacuum grease. The EBW-pellet assemblies were then secured using a 3D printed fixture within a steel fragment chamber that had a 6.35 mm thick polycarbonate viewing window. The polycarbonate windows were cracked after each experiment and had to be replaced. A Fujikura FIGH-10-500N imaging fiber with 10,000 imaging elements (nominal) (Figure 2A) with an SMA connector was attached to a Thorlabs F220SMA-A lens with a focal length of 10.92 mm. A 2 mm spacer was used between the fiber SMA end and the lens to facilitate focusing at a distance of 13 mm from the lens front surface to form an image on the imaging fiber end. The other side of the fiber was coupled to an Olympus 40 \times microscope objective in an adjustable extension tube, which produced a magnified image on the image intensifier photocathode. The resulting field of view was approximately 2.5 mm by 2.5 mm. The image intensifier phosphor screen was imaged using a Phantom V7.3 black and white camera at a frame rate of 1 Hz at the maximum exposure of 0.9996 s with a window size of 800 by 600 pixels (Figure 2B). The image intensifier was an 18 mm MCP Gated Image Intensifier with an S20 cathode and a P43 phosphor used in Stanford Computer Optics 4 Quick 05 A cameras. A pulse generator was used to provide a single externally triggered 10 ns wide gating pulse from a +2 V positive bias pulled down to -8 V to prevent electron generation prior to the pulse. Two separate high voltage power supplies were used to provide an MCP voltage of 900 V and an 8 kV bias voltage. For initial sample alignment and images before testing, the pulse generator was triggered at 10 Hz continuously with an intensifier gate of 1 ms at the same settings. A linear Hall Effect current sensor was used to detect the change in current from the capacitive discharge unit (CDU) that initiated the EBW, which was used to trigger an oscilloscope and a Stanford DG535 delay generator. The delay generator was programmed to send a trigger pulse to the pulse generator after a specified delay time which is based on a combination of the measured break-out time of the detonator after initiation ($2.75 \mu\text{s} \pm 25 \text{ ns}$), the inherent time delay, and jitter in the pulse generator ($200 \pm 25 \text{ ns}$) and the estimated time for the detonation wave to reach the observed location on the samples calculated from the detonation speed in the sample. A trigger pulse from the

oscilloscope was also sent to a Shimadzu HPV-X2 camera, which was used to record 10 million frames per second (Mfps) video of the detonation event at a larger field of view at reduced resolution ($97 \mu\text{m}/\text{pixel}$) for a total of 256 frames ($25.6 \mu\text{s}$ total recording time) (Figure 2C). The camera window size was 400 by 260 pixels, but in this mode, the camera obtains interlacing frames from half of the rows during each frame acquisition and interpolates them. For these settings, the exposure time is fixed at 50 ns.

3 Results and Discussion

The images from the experiment with the HMX ($R=3 \text{ mm}$, $H=6 \text{ mm}$) pellet are shown in Figure 3, including the low-resolution image before the test (Figure 3A), series of low-resolution images (Figure 3B) showing the detonation front at the same time as the high-resolution image was captured ($t=0$) and the subsequent air shock, schematic for the detonation front (Figure 3C), high-resolution images (Figure 3D) before and (Figures 3E) during the experiment. The selected area was approximately 1.5 mm below the top surface and near the center of the pellet. There were two 1 mm size HMX particles placed on top of the pellet, one near the front-facing camera, and another at the other farther end (Figure 3B, $t=+0.2$, white arrows), to aid in focusing during initial alignment for the high-magnification images. The lower resolution image captured at the same location (Figure 3B, $t=0$) shows a bright detonation front within the solid pellet as compared to the products that appear dark. The motion blur for the low-resolution image is $430 \mu\text{m}$ ($8.6 \text{ km/s} \times 50 \text{ ns}$), which is 4 pixels wide. The following images show the air shock formation at the top of the pellet after break-out and moving at a speed of around 10 km/s. One of the HMX particles that was initially placed on top of the pellet was also visible in later frames (Figure 3B, $t=+3.7$) indicating that it was ejected hypersonically at the same speed of 10 km/s.

The curved shock front depicted in Figure 3C causes break-out at the core of the pellet first. The air shock morphology was observed to follow the curved detonation front within the HE (Figure 3C). It should be noted that in this and the following figures, the air shocks were brighter than the detonation fronts due to the extremely high adiabatic heating with a range of estimated temperatures of 10000–20000 K [23–25]. The bright detonation front at the pellet front surface is near the bottom of the high-resolution frame (Figure 3E), and the light transmission ahead makes the unreacted section of the pellet visible. This diffuse light shows the outline of a few particles with their visible boundaries near the front. The bright rough zone is assumed to be the detonation front that corresponds to the HMX particle scale. The apparent average width of this bright front measured is $210 \mu\text{m}$, which when corrected for motion blur ($8.6 \text{ km/s} \times 10 \text{ ns} = 86 \mu\text{m}$) reduces to $120 \mu\text{m}$. The reported values for HMX reaction zone duration is on the order of 10–12 ns, which gives a width of 90–120 μm [26], consistent with this measurement. There is a

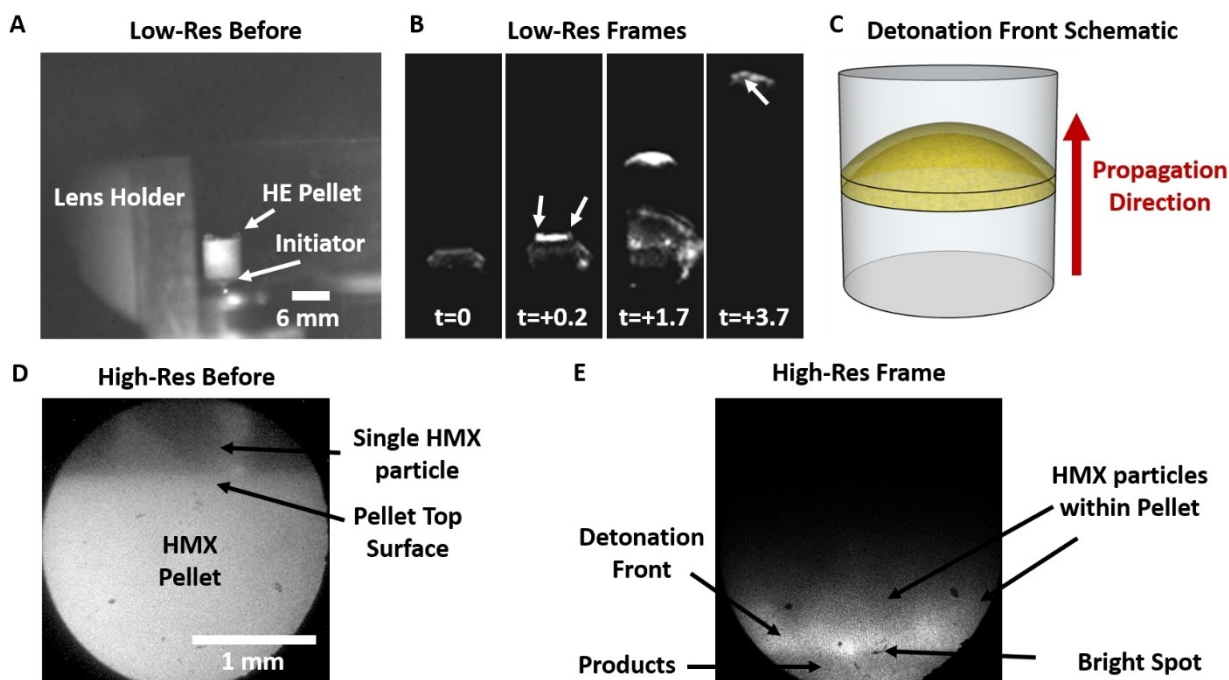


Figure 3. A. Low-resolution large field of the view camera image of the overall setup showing the lens holder for the imaging fiber and the HE pellet on top of an initiator behind a polycarbonate shield. B. The frame at the moment the high-resolution image was acquired is denoted as $t=0$. The next frame is at break-out $t+0.2 \mu\text{s}$ after the previous frame. The HMX particles on top of the pellet are visible (white arrows). Air shock after $t+1.7 \mu\text{s}$. Air shock with the ejected HMX particle (white arrow) visible $t+3.7 \mu\text{s}$. The HMX particle did not appear to detonate. Both the air shock and the particle speeds are near Mach 30. C. The schematic detonation front geometry within the pellet. The front is ahead at the core of the pellet due to the curvature of the front. D. The high-resolution image of the pellet before the experiment. The HMX particle at the top surface was used for focusing. E. The high-resolution single frame acquired showing the detonation front and a bright spot at a possible particle boundary. The illumination ahead of the detonation front is due to the diffuse emitted light from the detonation front, which delineates the particle boundaries in the pressed pellet.

brighter spot discernible at the bottom of the particle near the image center suggested by the round particle outline. The spot might form from an air shock within a pore between particles near the surface suggested by its relative brightness. The products behind the front appear much darker due to the lower emissivity of expanding gaseous species, visible in both low and high-magnification images.

The next set of experiments refer to three PBX 9501 pellets with 500 μm diameter holes imaged at increasing trigger delays. Figure 4 shows the low and high-magnification images from the PBX 9501 pellet before (Figure 4A) and during detonation (Figure 4B,C,D). Two of the samples had ink markers located next to the holes, which helped with focusing but also to determine if the detonation front has passed across those locations (Figures 4A, B, D). The prismatic shape of the pellet helps demonstrate the front curvature that is not discernible in a cylindrical geometry due to the radial symmetry (compare Figure 3C and 6A). The detonation failure diameter of PBX 9501 is 1.6 mm, so these samples were not close to failure [27]. The low and high-magnification frames are approximately matched, but the low magnification 10 Mfps images have a motion blur of about 4 pixels wide over the 50 ns exposure. As the detonation front reaches the through-hole, it

breaks out along its lower periphery at the core of the pellet first due to the curvature of the front ($\sim 1 \text{ mm}$ high over a distance of 3 mm between the center and the surface). The break-out and resulting material jetting in a hole geometry has been observed in inert materials [28] and modeled by employing numerical simulations with similar results [29–31].

The visible intact ink marks on the surfaces (Figure 4B, D) indicate that the detonation front has not reached the hole located at the surface. The brightness also increases and reaches a maximum farther below the hole as the diffuse light from the detonation has to travel a shorter path through the pellet towards the camera. The illumination from the collapsed hole is in line with numerical simulations that predict such hot zone formation upon impingement of the air shock and possible jets impinging the opposite surface. It is expected that the hot products are ejected out of the hole in the direction of the camera and Figure 5 shows the progression of this jetting at low resolution marked by the white arrows.

The location of a distinct band at the surface of the pellets can be seen on Figure 4D with the longest trigger delay and the detonation front on the surface has almost reached the location of the hole, evidenced by the missing lower part of

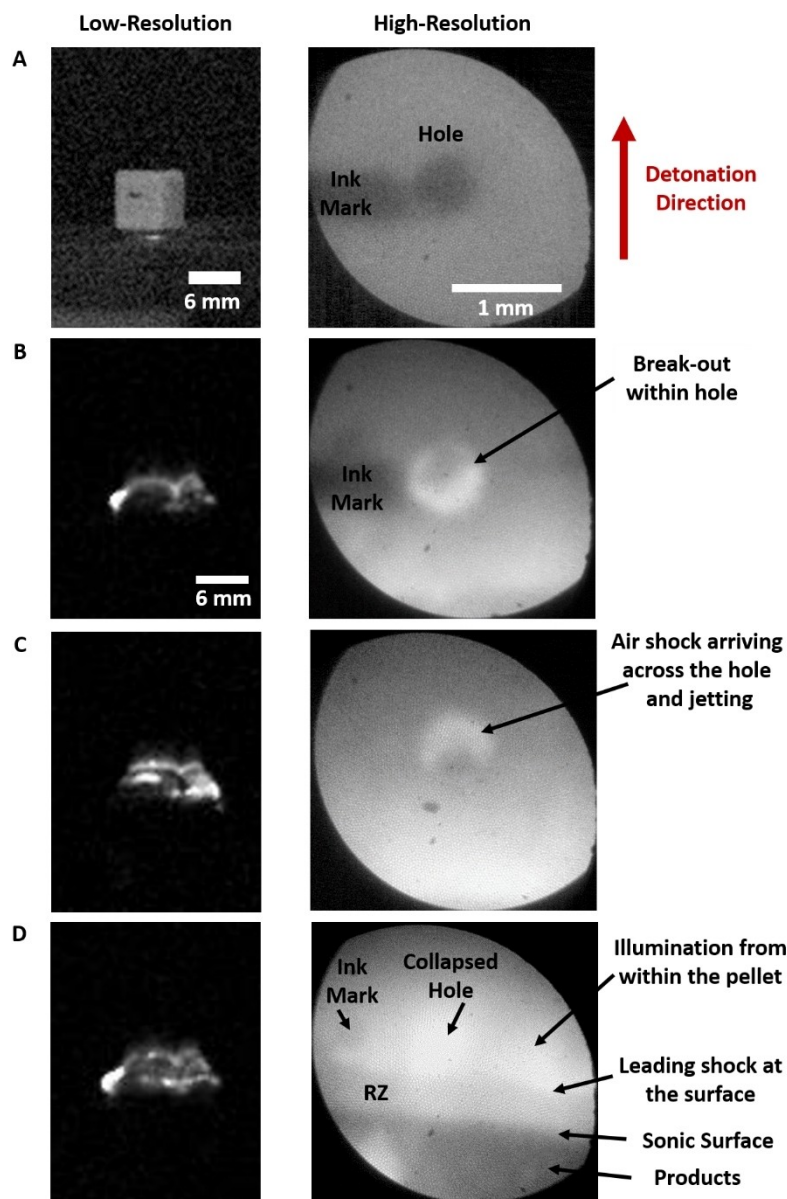


Figure 4. A. Low-resolution large field of the view camera image of one of the PBX 9501 HE prism pellets on top of an initiator before the experiment. The ink mark next to the hole is visible on the pellet and the corresponding high magnification image. B. The low and high-resolution frames showing the curved detonation front and the bright hole. The front is ahead at the core of the pellet by about 1 mm due to the front curvature and the leading shock locations at the core and the surface of the pellet are marked. The break-out within the hole is visible. The illumination ahead of the DDZ at the surface is due to the diffuse emitted light from the core of the pellet. C. A pellet with a longer time delay, where the curved detonation front has just passed over the hole at the core of the pellet. The high-resolution single-shot image shows the bright air shock impinging at the opposite side of the hole and the detonation front locations at the core and the surface of the pellet are marked. D. A pellet with a longer time delay showing the collapsed hole, the DDZ at the surface and the products which appear dark. The width of the detonation front is approximately 210 μm after correcting for motion blur. The ink mark on the surface is partially destroyed. The products show bright cellular structures.

the ink mark that was used. The width of this zone was wider compared to the pure HMX, approximately 210 μm after correcting for motion blur, although the detonation speeds are close (8.6 vs 8.4 km/s). This zone does not appear to have any significant substructure, variation in brightness, or show any signs of reaction progress across but it had distinct bounda-

ries. The reported RZ values for PBX 9501 is 130–170 μm measured using velocity interferometry system for any reflector (VISAR) [32]. It is computationally predicted that the RZ thickness would be larger at a weak confiner interface compared to the center of the HE [6, 10]. The measurements here are taken from the front surface, where there is only air con-

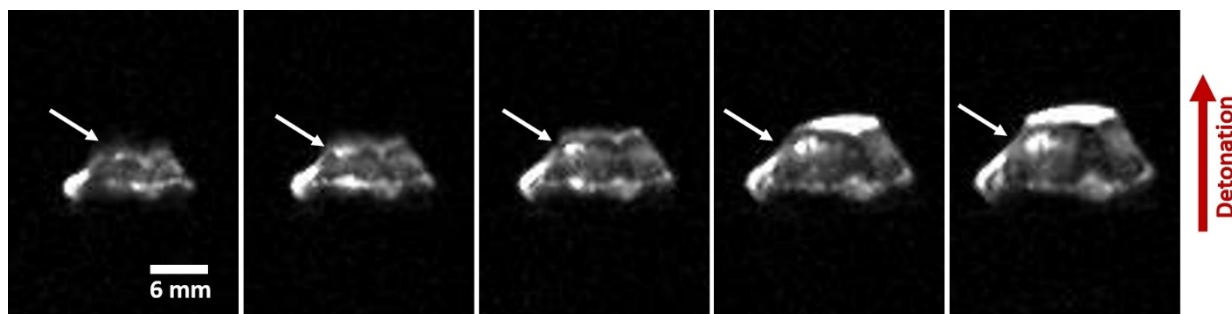


Figure 5. Jetting from the hole in a PBX 9501 pellet is marked by the white arrows, where each frame is separated by 100 ns.

finement, so these observations are consistent with computational predictions and prior observations that this zone is the RZ. No distinct bright spots were observed in the PBX9501 samples unlike HMX, which might be due to lack of voids in this sample that had lower porosity (2% vs 5%). The products behind this zone appear dark and exhibit some cellular substructure. A bright area was also visible within the products near the lower left part of the image. Such bright areas were visible in the prior frames at low resolution and might originate from the air shock near the pellet surface. One advantage of the high-resolution image was that the roughness of the zone was discernible, which can be related to the pellet microstructure, where the particle sizes are finer in PBX 9501. In general, results similar to the ones presented here can help improve reaction models for high explosives for more accurate predictions on reaction mechanisms and microstructural effects.

Figure 6 shows the schematic (Figure 6A) and the results from the interface experiment with the high-magnification images from the PBX 9501 pellet (right)-Sylgard 184 (left) before (Figure 6B) and during the experiment, one with the original frame with improved contrast (Figure 6C) and the same image marked with the different regions (Figure 6D). The camera was focused at the boundary to observe both the front structure within PBX 9501 and to measure the angles between the interface and the shock front and the material interface. The schematic for the explosive-confiner interface in the experiment shows the relevant geometry and angles. The curvature of the detonation front in PBX9501 is much more pronounced at the edge of the pellet, compared to the previous figures taken near the center of the pellet. The angle ω between the detonation front and the interface is approximately 62° . On the inert confiner side, the shock front is not visible as the current setup relies on emitted light from the sample. The material interface (i.e. streamline turning) angle θ is measured as 21° . The image shows that the width of the zone is unaffected and is nearly identical to the one in Figure 4D. This is because the observed front surface is under weak air confinement in the direction of the camera. A Prandtl-Meyer (PM) fan is also visible starting at the interface, and the schematic of the boundaries is shown in Figure 6A. PM fan is a supersonic expansion of the flow around a convex corner. It occurs as the

shock cannot turn at an angle isentropically and instead turns progressively in infinitesimal steps with a corresponding increase in Mach number up to a limiting value [33].

These measured angles permit the optical determination of the pressure at the intersection point (which is a line in the depth direction) of an inert confiner interface and a detonation shock (Figure 6A) using shock polar analysis and the properties of the HE. The shock polar equations relate the angles and pressures at interfaces between an explosive and a confiner using the driving shock speed and the phase velocity at the interface along with material properties and their equation-of-states (EOS's). The application of shock polar analysis for explosive-confiner interactions has been developed in the past [19,20] and the following discussion closely follows from these sources. Although the discussion below assumes an ideal gas behavior at the strong shock limit to simplify the analysis, the approach applies to any type of EOS. A typical confiner-explosive interface is shown in Figure 6A. For an ideal gas in the strong shock limit, the pressure and streamline turning angle are given by:

$$p = \frac{2\rho_0 D_0^2 \cos(\omega)^2}{\gamma + 1}$$

$$\theta = \arctan \frac{2\sin(\omega)\cos(\omega)}{\gamma + 1 - 2\cos(\omega)^2}$$

where ρ_0 is the initial density, D_0 is the phase speed, ω is the angle between the interface and the shock front and γ is the specific heat ratio. For the case of PM expansion fan formation, the streamline turning angle θ is related to the Mach number M and the corresponding pressure after the turn with the Prandtl-Meyer function:

$$\theta = \sqrt{\frac{\gamma+1}{\gamma-1}} \arctan \sqrt{\frac{\gamma-1}{\gamma+1}} (M^2 - 1) - \arctan \sqrt{M^2 - 1}$$

using the fact that the initial Mach number M_0 is 1 since the PM fan wave head starts at the sonic locus at the interface and

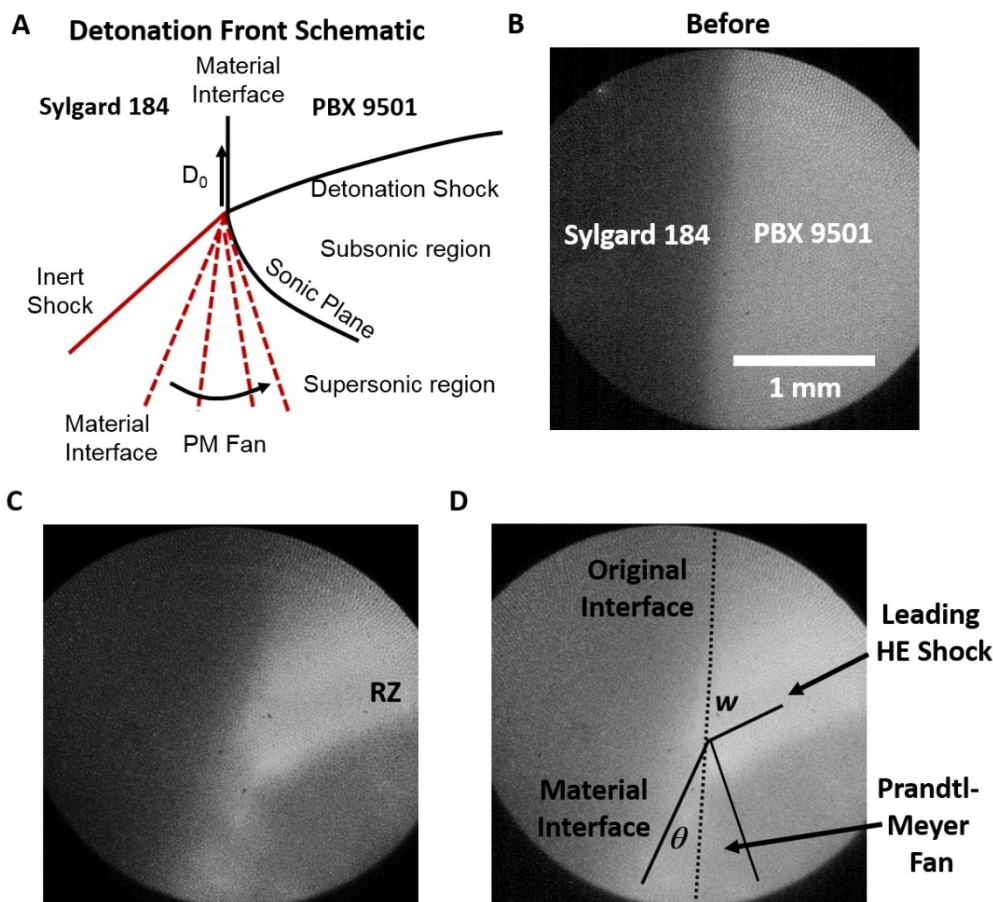


Figure 6. A. The detonation front and shock wave schematic at the interface between an HE pellet and an inert confiner. The high-magnification images of the interface between the PBX 9501 pellet and a Sylgard 184 block B. before and C, D during the passage of the detonation front. The image is used to measure the leading shock angle in the HE and the streamline deflection (i.e. material interface) angle. A Prandtl-Meyer expansion fan is also visible. The leading shock in the inert material was not visible.

$$p = p_s \left(\frac{1 + \frac{\gamma-1}{2} M^2}{1 + \frac{\gamma-1}{2} M^2} \right)^{\frac{\gamma}{\gamma-1}}$$

where p_s is the pressure at the sonic locus ($M=1$). These sets of equations can be used to calculate and plot the pressure and streamline deflection angle θ using the angle w as a parameter varying between 0 and 90°. Using $D_0=8.4$ km/s, $\rho_0=2$ g cm⁻³ and $\gamma=3$ for PBX 9501 and $D_0=8.4$ km/s, $\rho_0=1.03$ g cm⁻³ and $\gamma=1.4$ and 2.3 for the inert Sylgard 184 material, the shock polars for the case here can be constructed as shown in Figure 7A.

In general, there are many different possibilities for shock polar matching depending on the properties of the confiner material, where the shock polars directly cross at multiple points. Furthermore, it has been noted that the matching condition can depend on the thickness of the confiner in relation to the explosive critical radius if multiple solutions are possible [19]. The matching can also be determined based on the morphology of the material interface and the streamline de-

flection angle θ if these can be directly observed, as in the direct imaging approach here. For the case presented here with the PM fan, the angles in Figure 6A allow a single point where the polar matching is possible as shown on Figure 7A with the circle marker, uniquely identifying the pressure at the intersection between the inert confiner material and the detonation front. Using the streamline deflection angle and the PM fan polar for PBX 9501, the pressure in Sylgard 184 can be calculated as 24.5 GPa at the boundary. Using the Sylgard 184 calculated shock polar instead, pressure from the shock polar matching conditions is 16 GPa for $\gamma=1.4$ although this does not match the measured θ (25 vs 21°). A value of $\gamma=2.8$ for Sylgard 184 provides a better match (Figure 7A). This is not surprising since $\gamma=1.4$ is for an ideal gas and it increases for non-ideal gases, such as those that would originate from the decomposition of solids ($\gamma=3$ is typically used for HE). This data point gives u_p - U_s values of 3.4 and 6.9 km/s using shock equations and the hugoniot for an ideal gas EOS [34], which compares well with published Sylgard 184 shock hugoniot data obtained by ultrafast time-domain interferometry (UTDI)

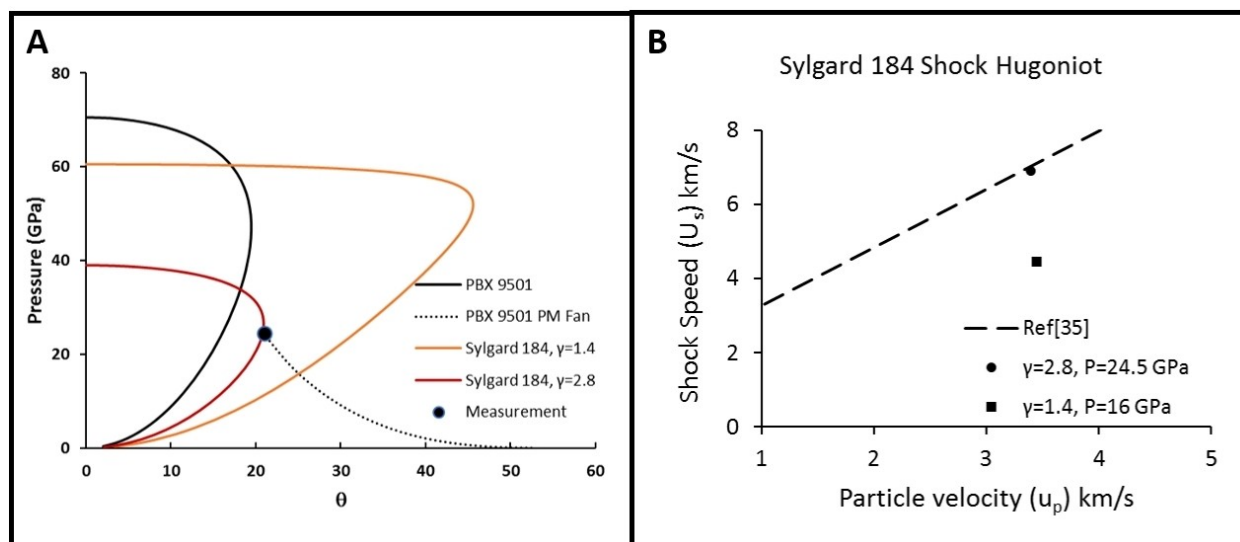


Figure 7. A. The calculated shock polars for PBX 9501 and Sylgard 184 with two specific heat ratios (γ) 1.4 and 2.8 along with the experimental optical measurement marked by the circular marker. B. Shock Hugoniot data comparison between the measured value and prior data from [35].

and gas gun experiments ($U_s = 1.57u_p + 1.70$ km/s) [35] (Figure 7B). The same approach can be used to not only optically measure pressure within a heterogeneous material under shock from a known HE, but it can also be used to determine material properties and EOS with multiple experiments by varying the shock pressure, especially for the high-pressure regime. For example, by using explosive pellets pressed to different densities in multiple experiments, it is possible to fit the EOS and Hugoniot parameters in more advanced models for an unknown material rapidly in a few simple small-scale experiments. This is a highly attractive approach to complement the existing 1D methods such as plate impact experiments using diagnostics such as photonic Doppler velocimetry (PDV), VISAR, or UTDI with 2D data, especially for heterogeneous materials.

4 Conclusions

This work reports on a new diagnostic method that allows microscopic imaging of self-supported detonations in high explosive (HE) pellets of HMX and PBX9501. The system uses an imaging fiber coupled to an image intensifier to provide high-resolution (15 μm) short-exposure (10 ns) images. The images revealed features such as bright spots, pore collapse in engineered holes, hypersonic particle ejection and air shocks, reaction zone (RZ) morphologies, and thicknesses. The RZ exhibited roughness proportional to the particle dimensions. The RZ thickness on the free surface of HMX and PBX 9501 pellets were measured as 120 and 210 μm respectively. The bright spot observed in the HMX pellet within the RZ was trailing the leading shock and was near the sonic surface and the brightness level suggests it was formed by air shock and the associated adiabatic heating. Single HMX particles placed

on top of the pellet were ejected at 10 km/s, traveling with the air shock without a sign of initiation. The RZ in PBX9501 was smoother and showed no brightness variation across suggestive of reaction progress, temperature, or pressure gradient. The morphology of the break-out and collapse of engineered 500 μm diameter through-holes were observed in three-time steps, showing the air shock and the ejecta at different stages, which showed consistent features with past numerical simulations. The interface between prisms of inert Sylgard184 and PBX9501 was imaged during the detonation event to determine the pressure optically using shock polar analysis by measuring the detonation front angle and the streamline deflection angle. The interface showed a Prandtl-Meyer fan and the pressure at the interface was calculated as 24.5 GPa and a specific heat ratio of 2.8 provided the best match for the Sylgard 184 gaseous products. The same methodology can be used to determine any form of equation-of-state and Hugoniot curves for arbitrary materials using a few relatively simple small-scale experiments.

Acknowledgments

This work was supported by the Air Force Office of Scientific Research (AFOSR), Dynamic Materials and Interactions program (Grant No.: FA9550-15-1-0202, Program Manager: Dr. Martin Schmidt, Dr. Jennifer Jordan), AFOSR DURIP Grant FA9550-18-1-0518 (Program Manager: Dr. Martin Schmidt). We would like to thank Vasant Vupuluri for preparing samples and helping with experiments, Caitlin O'Grady for drilling the holes, Steve Son for his support, and Terry Meyer and Weinong Chen for the use of the Shimadzu camera.

Data Availability Statement

No data available.

References

- [1] F. P. Bowden, A. D. Yoffe, *Initiation and growth of explosion in liquids and solids*. Cambridge University Press, The Pitt Building, Trumpington Street, Cambridge CB2 1RP, UK, **1952**.
- [2] C. H. Johansson, P. A. Persson, *Detonics of High Explosives*. Academic Press, London, New York, **1970**.
- [3] A. W. Campbell, W. C. Davis, J. B. Ramsay, J. R. Travis, Shock initiation of solid explosives. *Phys. Fluids* **1961**, *4*, 511–521.
- [4] C. M. Tarver, S. K. Chidester, A. L. Nichols, Critical conditions for impact-and shock-induced hot spots in solid explosives. *J. Phys. Chem.* **1996**, *100*, 5794–5799.
- [5] C. A. Handley, B. D. Lambourn, N. J. Whitworth, H. R. James, W. J. Belfield, Understanding the shock and detonation response of high explosives at the continuum and meso scales. *App. Phys. Rev.* **2018**, *5*, 011303.
- [6] J. Bdzil, T. Aslam, R. Henninger, J. J. Quirk, High-explosives performance: understanding the effects of a finite-length reaction zone. *Los Alamos Sci.* **2003**, *28*, 96–110.
- [7] G. Sharpe, J. Bdzil, Interactions of inert confiners with explosives. *J. Eng. Mater. Technol.* **2006**, *54*, 273–298.
- [8] W. Fickett, W. Davis, *Detonation*. University of California Press, Berkeley, **1979**.
- [9] J. W. Forbes, *Shock Wave Compression of Condensed Matter*. Springer-Verlag, Springer Heidelberg New York Dordrecht London, **2012**.
- [10] M. Short, J. J. Quirk, High explosive detonation-confiner interactions. *Annu. Rev. Fluid Mech.* **2018**, *50*, 215–242.
- [11] E. D. Eyles, High-speed photography and its applications to industrial problems. *J. Sci. Instrum.* **1941**, *18*, 175–184.
- [12] K. L. McNesby, B. E. Homan, R. A. Benjamin, V. M. Boyle, J. M. Densmore, M. M. Biss, Quantitative imaging of explosions with high-speed cameras. *Rev. Sci. Instrum.* **2016**, *87*, 051301.
- [13] A. S. Tappan, C. D. Yarrington, R. Knepper, Detonation corner turning in vapor-deposited explosives using the micromushroom test. *AIP Conf. Proc.* **2018**, *1979*, 100041.
- [14] I. Plaksin, J. Campos, J. Ribeiro, R. Mendes, Detonation phenomena of PBX microsamples. *AIP Conf. Proc.* **2002**, *620*, 918.
- [15] I. Plaksin, J. Ribeiro, R. Mendes, S. Plaksin, L. Rodrigues, J. Campos, M. Herrmann, I. Mikonsaari, H. Krause, Exploring the HMX-based PBXs with the TATB shock sensitivity. *Insensitive munitions and energetic materials technology symposium*. **2012**.
- [16] T. Aslam, S. Jackson, J. Morris, Proton radiography of PBX 9502 detonation shock dynamics confinement sandwich test. *AIP Conf. Proc.* **2009**, *1195*, 241–244.
- [17] B. R. Breed, D. Venable, Dynamic observations of the course of a shock-induced polymorphic phase transition in antimony. *J. Appl. Phys.* **1968**, *39*, 3222.
- [18] N. D. Parab, Z. A. Roberts, M. H. Harr, J. O. Mares, A. D. Casey, I. E. Gunduz, M. Hudspeth, B. Claus, T. Sun, K. Fezzaa, S. F. Son, W. W. Chen, High speed x-ray phase contrast imaging of energetic composites under dynamic compression. *Appl. Phys. Lett.* **2016**, *109*, 131903.
- [19] T. D. Aslam, J. B. Bdzil, Numerical and theoretical investigations on detonation-inert confinement interactions. *12th Symposium (International) on Detonation*, San Diego, CA, USA, August 11–16, **2002**, 1195, 483–488.
- [20] T. D. Aslam, J. B. Bdzil, Numerical and theoretical investigations on detonation confinement sandwich tests. *13th Symposium (International) on Detonation*, Norfolk, VA, USA, July 23–8, **2006**, 761–769.
- [21] J. L. Brown, G. Ravichandran, Analysis of oblique shock waves in solids using shock polars. *Shock Waves* **2014**, *24*, 403–413.
- [22] J. L. Brown, G. Ravichandran, W. D. Reinhart, W. M. Trott, High pressure hugoniot measurements using converging shocks. *J. Appl. Phys.* **2011**, *109*, 093520.
- [23] C. Park, Assessment of two-temperature kinetic model for ionizing air. *J. Thermophysics* **1989**, *3*, 233–244.
- [24] W. C. Davis, T. R. Salyer, S. I. Jackson, T. D. Aslam, Explosive driven shock waves in argon. *13th Symposium (International) on Detonation*, Norfolk, VA, USA, July 23–28, **2006**, 1035–1044.
- [25] N. Glumac, Early time spectroscopic measurements during high-explosive detonation breakout into air. *Shock Waves* **2013**, *23*, 131–138.
- [26] C. M. Tarver, Detonation reaction zones in condensed explosives. *AIP Conf. Proc.* **2006**, *845*, 1026.
- [27] A. W. Campbell, R. Engelke, The diameter effect in high-density heterogeneous explosives. *6th Symposium (International) on Detonation*, Coronado, CA, USA, August 24–27, **1976**, 642–652.
- [28] J. Dear, J. Field, A. J. Walton, Gas compression and jet formation in cavities collapsed by a shock wave. *Nature* **1988**, *332*, 505.
- [29] L. Tran, H. S. Udaykumar, Simulation of void collapse in an energetic material, part 2: Reactive case. *J. Propul. Power* **2006**, *22*, 959–974.
- [30] N. K. Rai, H. S. Udaykumar, Void collapse generated meso-scale energy localization in shocked energetic materials: Non-dimensional parameters, regimes, and criticality of hotspots. *Phys. Fluids*. **2019**, *31*, 016103.
- [31] C. Li, B. W. Hamilton, A. Strachan, Hotspot formation due to shock-induced pore collapse in 1,3,5,7-tetranitro-1,3,5,7-tetrazoctane (HMX): Role of pore shape and shock strength in collapse mechanism and temperature. *J. Appl. Phys.* **2020**, *127*, 175902.
- [32] R. L. Gustavsen, S. A. Sheffield, R. R. Alcon, Detonation wave profiles in HMX based explosives. *AIP Conf. Proc.* **1998**, *429*, 739–742.
- [33] J. D. Anderson, Hypersonic and High Temperature Gas Dynamics. AIAA, **2000**.
- [34] S. B. Segletes, An Analysis on the Stability of the Mie-Grüneisen Equation of State for Describing the Behavior of Shock-Loaded Materials. *Technical Report BRL-TR-3214*, **1991**.
- [35] B. A. Jilek, I. T. Kohl, D. A. Farrow, J. Urayama, R. Knepper, G. Radtke, S. P. Kearney, M. R. Armstrong, J. C. Crowhurst, J. Lewicki, K. M. Coleman, J. M. Zaug, Unreacted Equations of State of Sylgard and Hexanitroazobenzene (HNAB) Determined by Ultrafast Time Domain Interferometry. *15th Symposium (International) on Detonation*, San Francisco, CA, USA, July 13 –18, **2014**, 437–444.

Manuscript received: December 29, 2020

Revised manuscript received: April 20, 2021

Version of record online: June 24, 2021